Black Phosphorus-Based Surface Plasmon Resonance Biosensor for DNA Hybridization

Rajeev Kumar, *Member, IEEE*, Shivam Singh, Bhargavi Chaudhary, *Graduate Student Member, IEEE*, and Santosh Kumar, *Senior Member, IEEE*

***Abstract*— In this work, we proposed and performed the numerical analysis of novel surface plasmon resonance (SPR) biosensor architecture (Prism-BAK1/Ag/WS_2/Ni/BP/SM) based on angular interrogation at a wavelength of 633 nm. At minimum reflectance (R_{min}) value, the remarkable sensitivity and figure of merit (FoM) of 198.15°/RIU and 64.79/RIU are attained at a refractive index (RI) range of 1.33–1.41 for the sensing medium (SM). Additionally, the performance parameters of the SPR biosensor are meticulously measured in relation to FoM, sensitivity, limit of detection (LoD), and detection accuracy (DA) concerning the concentration of complementary target DNA hybridization in the SM. The maximum sensitivity is achieved with DNA hybridization. Notably, the probe and mismatch DNA hybridization demonstrate the maximum sensitivities of 379.69°/RIU and 383.01°/RIU, respectively. Thus, this structure-based SPR biosensor can distinguish between single nucleotide polymorphism (SNP) and DNA hybridization. In the realm of biomedicine, this adaptable biosensor holds great potential for the detection of life-threatening diseases through DNA hybridization.**

***Index Terms*— Biosensor, black phosphorus, DNA hybridization, sensitivity, surface plasmon resonance (SPR).**

I. Introduction

THE field of advanced detection technologies has shown considerable interest in surface plasmon resonance (SPR) sensor optical bioinstrumentation due to its promising applications across various domains. These applications encompass medical diagnostics, environmental monitoring, as well as the detection of biomolecules and substances [1], [2], [3]. Specifically, in the binding processes involving proteins and DNA–DNA hybridization, this technology has proven its value by monitoring a large range of biochemical interactions [4], [5], [6], [7]. SPR technology investigates binding interactions between a biomolecule and an analyte in a label-free technique by acting as an optical display [8], [9], [10]. Surface plasmons (SPs) are generated along the interface between metal–dielectric due to charge density oscillation [11], [12], [13]. SPs represent a strong technique for detecting changes in a sample's refractive index (RI) due to binding interactions. Their utility in biosensing applications stems from their propagation dependence on the effective RI (ERI) of the sensing medium (SM) adjacent to the metal layer. When the incident light meets certain criteria, particularly when directed by a pronounced reflectance dip, SP waves (SPWs) are excited [14]. Because the complex RI in the metal coating interface, the nearby sensing dielectric layer, and their geometric configurations all affect the SPWs optical excitation, these factors can significantly alter both the propagation constant and this reflectance dip. For generation of the SPs, metals, such as gold (Au), copper (Cu), and silver (Ag), are frequently employed [15], [16]. Au and Ag are particularly effective for creating robust plasmonics. Nevertheless, these metals, especially Ag, are prone to oxidation. To counteract metal oxidation and improve performance, a 2-D material layer is employed [17], [18], [19], [20]. High reliability and specificity characterize SPR-based optical biosensors, making them widely utilized in biological and biochemical detection [14], [21], [22], [23]. In recent times, there has been a growing interest in utilizing this biosensor architecture for medical diagnostic applications. Biochemical processes, such as the bond between adenine (A) and thymine (T) or between guanine (G) and cytosine, are included in its hybrid architectures, effectively merging medical diagnosis with optical interactions. The two operating modes of the attenuated total reflection method-based SPR biosensor are wavelength inquisition, in which the wavelength of the incident light signal is varied while the incident angle is fixed, and angular inquisition, in which the incident angle is fixed while the wavelength is varied. Incorporating both MoS_2 and graphene into the enhancement layer of a single sensor design leads to a significant improvement in the performance of SPR sensors [24], [25], [26]. Protein–DNA interactions, food safety monitoring, biological sensing, beam polarization selection, and other sensing applications are just a few of the many uses for these SPR sensors [27], [28], [29], [30]. They are also used in interactions between proteins, enzymes, substrates, and inhibitors, along with DNA-DNA hybridization

Manuscript received 10 March 2024; revised 28 March 2024; accepted 2 April 2024. The review of this article was arranged by Senior Editor S. J. Gitomer. *(Corresponding authors: Bhargavi Chaudhary; Santosh Kumar.)*

Rajeev Kumar is with the Department of Electronics and Communication Engineering, Graphic Era (Deemed to be University), Dehradun, Uttarakhand 248002, India (e-mail: rajeevkrc@gmail.com).

Shivam Singh is with the Department of Electronics and Communication Engineering, ABES Engineering College, Ghaziabad, Uttar Pradesh 201009, India (e-mail: shivams20@gmail.com).

Bhargavi Chaudhary is with the Department of Electrical Engineering, Indian Institute of Technology, New Delhi 110016, India (e-mail: bhargavichy31@yahoo.com).

Santosh Kumar is with the Department of Electronics and Communication Engineering, Koneru Lakshmaiah Education Foundation, Vaddeswaram, Andhra Pradesh 522302, India (e-mail: santosh@kluniversity.in).

Color versions of one or more figures in this article are available at https://doi.org/10.1109/TPS.2024.3386399.

Digital Object Identifier 10.1109/TPS.2024.3386399

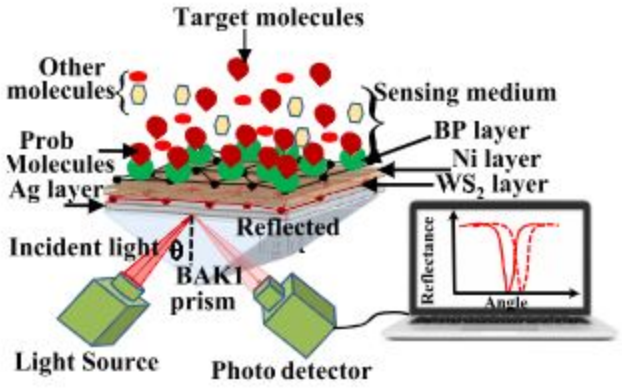

Fig. 1. Experimental setup for the proposed DNA hybridization.

and early cancer cell detection. Being 2-D materials with monoatomic thickness, both MoS_2 and graphene have several beneficial properties, such as high carrier mobility, high optical transparency, and tunability in addition to particular low reluctance. It has been established through both theoretical and experimental methods that these materials can be used to excite SPs.

In this work, an optimized BAK1/Ag/WS_2/Ni/BP-based SPR biosensor structure is utilized for DNA–DNA hybridization. Because of the electric field that surrounds WS_2, Ni, and BP, these materials are highly responsive to charged analytes, such as ions, DNA, and body cells, which makes them perfect for building high-performance biosensors. This is explained by the theoretical finding that charge can be transferred via DNA bio-foci to BP surfaces when DNA adsorbs onto BP. The van der Waals bonding (π stacking) that forms between DNA bases and carbon atoms causes an abrupt shift in the RI close to the BP-sensing layer interface. The effects of increasing thickness of Ni layer are investigated, and it is found that at 22 nm thickness of Ni layer, the biosensor's performance parameters, such as sensitivity, limit of detection (LoD), and figure of merit (FoM), are improved. Reflectance curves are plotted for an increasing number of layers, and a comparison of biosensor's sensitivity and FoM is conducted with respect to step-by-step layers (conventional layer) and a previous study. Notably, the proposed biosensor with enhanced Ni layers demonstrates remarkable sensitivity along with improved FoM and LoD.

II. Proposed Biosensor Structure

Fig. 1 shows the six-layered proposed SPR biosensor. The initiation of SPs requires p-polarized incident light, necessitating the modification of the entrance path with a polarizer. The selected wavelength for the proposed biosensor is 633 nm as it exhibits minimal Kerr effect at this wavelength, leading its excellent overall performance. Based on the existing literature, the developed biosensor uses an angular interrogation technique and a Fresnel equation approach based on the Kretschmann arrangement.

A. RI of Constitute Layer

Here, BAK1 prism is used as a coupling device and having RI (n_1) 1.5704. The selection of the RI-based prism is deliberate as it shows smaller coupling losses and also suitable for biosensing applications. An SPR active silver metal layer is used on the BAK1 prism to generate SPs. Moreover, it shows the enhanced sensing performance in relation to sensitivity and FoM. Its RI (n_2) is estimated by the Drude–Lorentz model, given in (1). Additionally, the RI (n_4) of Ni layer is calculated by the same [31] as

$$n_m = \sqrt{\varepsilon_m} = \sqrt{1 - \frac{\lambda^2 \lambda_c}{\lambda_p^2 (\lambda_c + i * \lambda)}} \tag{1}$$

where $\lambda_p = 1.4541 \times 10^{-7}$ m and 2.5381×10^{-7} m and $\lambda_c = 1.7614 \times 10^{-5}$ m and 2.84092×10^{-5} m are the plasma and collision wavelengths of Ag and Ni layers, respectively. To achieve better sensitivity, we have optimized the thickness of Ag and Ni layer. Furthermore, to protect Ag layer from oxidation, the next layer is used WS_2 and having RI of $4.8937 + i{*}0.3124$ [32]. To protect Ni layer from oxidation, the next layer used is BP and having RI of $3.5 + i{*}0.001$ with 0.53 nm thickness [33]. For the detection of molecules, we employed an SM with an RI variation ranging from 1.33 to 1.41 [34]. In this case, the SM is utilized to carry the target DNA with a specific concentration. The addition of both bare and probe DNA (pDNA) to the detecting layer induces a change in the layer's RI. After absorbing DNA molecules, the detecting layer's ERI is accurately represented as follows [4], [5], [35], [36]:

$$n_{\text{sens}}^1 = n_{\text{sens}}^0 + c_a \times \frac{\Delta n}{\Delta c} \tag{2}$$

where n_{sens}^1 is the detecting layer's ERI following the absorption of DNA solutions and n_{sens}^0 is the detecting layers ERI prior to the absorption of DNA solutions.

The absorbed DNA concentration is denoted by c_a, and the RI progress caused by the DNA molecules is represented by $\Delta n/\Delta c$. When using water, the ERI development parameter ($\Delta n/\Delta c$) has a value of 0.18 ± 0.03 cm^3/gm. The changes in the detecting layers concentration (density) due to DNA immobilization detect the changes in SM of local RI (n_s), which is related by (2) [5], [37].

B. Mathematical Modeling

In this work, the intensity of reflected p-polarized incident light is computed through N-layer modeling. The transfer matrix method (TMM) is used to find the reflection coefficients because it is a precise technique that does not call for approximations. In the current investigation, there are many layers (n_k) layered stack along the z-axis. Notably, the proposed biosensor's thickness layers d_k, permeability μ_k, dielectric constant ε_k, and RIs of n_k are measured along the z-axis. The following is the relationship between the tangential component of the electric and magnetic fields between the first boundary, $Z = Z_1 = 0$, and the last boundary, $Z = Z_{N-1}$ [38], [39], [40], [41]:

$$\begin{bmatrix} U_1 \\ V_1 \end{bmatrix} = M \begin{bmatrix} U_{N-1} \\ V_{N-1} \end{bmatrix}. \tag{3}$$

The variables $[U_1\ V_1]$ and $[U_{N-1}\ V_{N-1}]$ consider the electric and magnetic fields at the first and last layer boundaries, and

M is the characteristics matrix, which has the following (3):

$$M = \prod_{k=2}^{N-1} M_k = \begin{bmatrix} m_{11} & m_{12} \\ m_{21} & m_{22} \end{bmatrix} \tag{4}$$

$$M_k = \begin{bmatrix} \cos\beta_k & -i\sin\beta_k/q_k \\ -iq_k\sin\beta_k & \cos\beta_k \end{bmatrix} \tag{5}$$

$$q_k = \sqrt{\frac{\mu_k}{\varepsilon_k}}\cos\theta_k = \frac{\sqrt{\varepsilon_k - n_1^2\sin^2\theta_1}}{\varepsilon_k} \tag{6}$$

$$\beta_k = \frac{2\pi}{\lambda} n_k \cos\theta_k (z_k - z_{k-1}) = \frac{2\pi d_k}{\lambda}\sqrt{\varepsilon_k - n_1^2\sin^2\theta_1} \tag{7}$$

where β_k represents the phase thickness and q_k represents as RI for the kth layer. The symbols of incident light wavelength and angle are represented by λ and θ_1, respectively.

The reflection coefficient (r_p) is given as follows:

$$r_p = \frac{(m_{11} + m_{12}q_n)q_1 - (m_{21} + m_{22}q_n)}{(m_{11} + m_{12}q_n)q_1 + (m_{21} + m_{22}q_n)} \tag{8}$$

where (6) is used to measure $[q_1, q_n]$ for the relative components of the first and nth layer, respectively. Equation (9) is used to measure the reflectance curve R for the N-layer model

$$R = |r_p|^2. \tag{9}$$

C. Performance Parameters

This section describes the mathematical formulas used to evaluate the sensor's performance parameters. The sensitivity is defined as the ratio between difference of the two resonance angle (i.e., $\Delta\theta_{res} = \theta_2 - \theta_1$) to the change in SM (i.e., $\Delta n_s = n_{s2} - n_{s1}$, where $n_{s1} = 1.33$, $n_{s2} = 1.41$, and $\Delta n_s = 0.08$). The full-width at half-maximum (FWHM) is a measure of difference between the 50% of the reflection intensity (i.e., $R_{min} = 0.5$). Detection accuracy (DA) is inversely proportional to the FWHM, and LoD is reciprocal of the sensitivity and multiplication of the error angle (0.001°). All performance parameters are the following formula [38], [39], [40], [41], [42]:

$$S = \frac{\Delta\theta_{Res.}}{\Delta n_s}(°/\text{RIU}) \tag{10}$$

$$\text{DA} = \frac{1}{\text{FWHM}}(1/°) \tag{11}$$

$$\text{FoM} = S \times DA(1/\text{RIU}) \tag{12}$$

$$\text{LoD} = \frac{\Delta n_s}{\Delta\theta_{res}} \times 0.001°(\text{RIU}). \tag{13}$$

III. Results and Analysis

A. Conventional SPR Biosensor Analysis Approach

Initially, we have discussed the effect of the optimized thickness of Ag layer on various sensor structures (Ag/SM, Ag/WS_2/SM, and Ag/WS_2/Ni/SM) having basic Kretschmann configuration. Ag metal layer is chosen as plasmonics. The crucial performance parameters, such as sensitivity and R_{min}, have been evaluated and graphically represented in Fig. 2. Fig. 2(a) shows the sensitivity variation at optimized thickness of Ag layer. For sensitivity measurement, the change in SM (Δn_s) of 0.08 is considered for conventional sensor. The measured sensitivity for three different sensors (Ag/SM, Ag/WS_2/SM, and Ag/WS_2/Ni/SM) varies from 55.82°/RIU to 112.76°/RIU, 104.25°/RIU to 122.24°/RIU, and 139.52°/RIU to 196.75°/RIU. Notably, the addition of the WS_2 and Ni layers results in an increase in sensitivity, as depicted in Fig. 2(a). After the optimization of Ag layer thickness, the sensitivities of 111.86°/RIU, 120.08°/RIU, and 185.18°/RIU are obtained at 51, 48, and 46 nm of Ag thickness at R_{min} value. The variation in minimum reflectance (R_{min}) is plotted at 1.33 and 1.41 RIs of SM, as depicted in Fig. 2(b) and (c). The R_{min} value initially decreases at a specific thickness

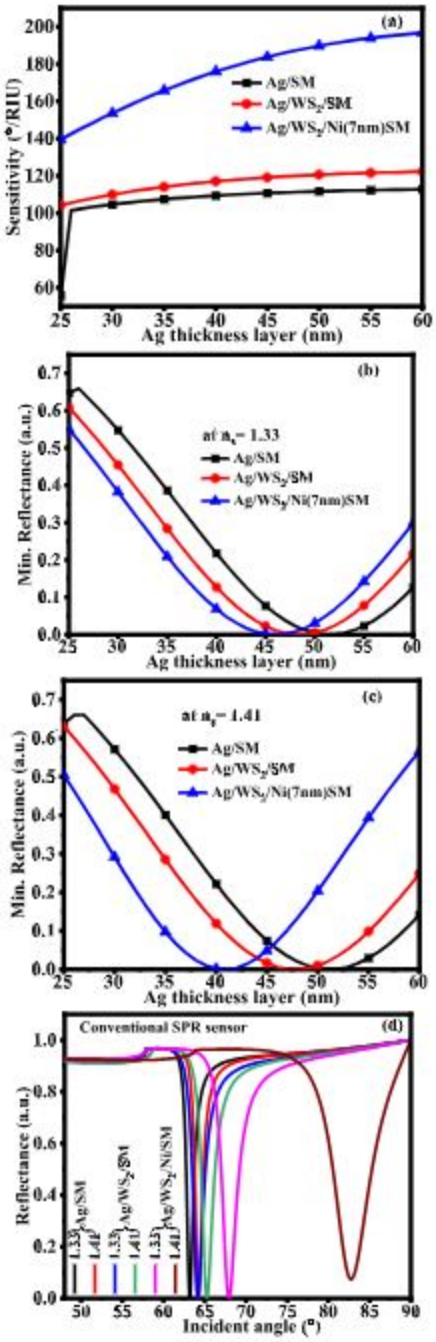

Fig. 2. Conventional SPR sensor with step-by-step layer. (a) Sensitivity. (b) R_{min} at $n_s = 1.33$. (c) R_{min} at $n_s = 1.41$. (d) Reflectance curve at R_{min} value at $n_s = 1.33$.

TABLE I
MEASURED PERFORMANCE PARAMETERS AT R_{min} WITH CONVENTIONAL SENSOR

Structure	S (°/RIU)	R_{min} (a.u.) at RI of SM		FWHM (°)	DA (/°)	FoM (/RIU)	LoD (RIU)
		1.33	1.41				
BAK1/Ag(51nm)/SM	111.86	4.7×10^{-4}	4.3×10^{-5}	1.01	0.99	110.74	8.9×10^{-6}
BAK1/Ag(48nm)/WS_2/SM	120.08	3.7×10^{-4}	8.5×10^{-5}	1.62	0.61	73.24	9.6×10^{-6}
BAK1/Ag(46nm)/WS_2(0.80nm)/Ni(7nm)/SM	185.18	7.6×10^{-4}	7.3×10^{-2}	2.22	0.45	83.33	5.4×10^{-6}

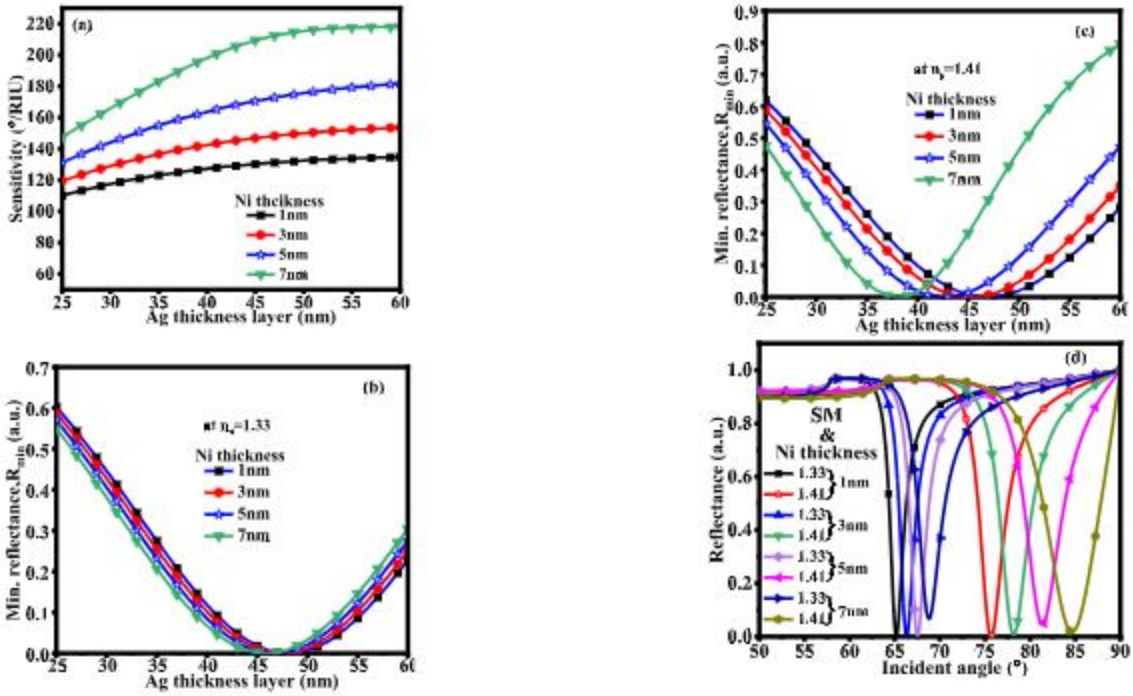

Fig. 3. Change in sensitivity and R_{min} value versus Ag optimized thickness. (a) Sensitivity. (b) R_{min} at $n_s = 1.33$. (c) R_{min} at $n_s = 1.41$. (d) Variations in reflectance curve versus incident angle at R_{min} value.

and subsequently rises for both SM. After adding WS_2 and Ni layers to the conventional biosensor, it is observed that the R_{min} value shifts lower thickness of Ag layer. The reflectance curve of conventional biosensor with and without WS_2 and Ni layers is displayed in Fig. 2(d). The changes in resonance angle ($\Delta\theta_{res}$) of conventional biosensor are 8.94°, 9.60°, and 14.81°, respectively, at 51, 48, and 46 nm of Ag thickness. It is noted that the resonance angle is more shifted, then adding the WS_2 and Ni layer in the conventional biosensor. Additionally, after adding the WS_2 and Ni layer, the reflectance curve widened. The other performance parameters are calculated and displayed in Table I.

B. Proposed Biosensor Analysis Approach

We have numerically investigated the behavior of the proposed sensor structure (BAK1/Ag/WS_2/Ni/BP/SM) using TMM at 633-nm wavelength after adding the BP layer. Fig. 3(a)–(c) shows the variation in sensitivity and R_{min} value at the optimized thickness of Ag and Ni layers for both monolayers of WS_2 and BP.

In Fig. 3(a), it can be observed that the sensitivity increases with the thickness of the Ag and Ni layers. The sensitivity variation is from 110.10°/RIU to 134.79°/RIU, 119.37°/RIU to 153.61°/RIU, 131.26°/RIU, 181.67°/RIU, and 147.48°/RIU to 217.89°/RIU at 1, 3, 5, and 7 nm thicknesses of Ni layer, respectively. Additionally, at R_{min}, the sensitivities of 131.21°/RIU, 148.21°/RIU,172.75°/RIU, and 198.15°/RIU are achieved with Ag thicknesses of 47, 47, 47, and 40 nm, respectively, and Ni thicknesses of 1, 3, 5, and 7 nm and also calculated and displayed the other performance parameters, shown in Table II. In this case, the R_{min} value is plotted, as shown in Fig. 3(b) and (c). It is noted that the R_{min} value is first decrease at particular thickness and then increase for both SMs. For the SM $n_s = 1.33$, the R_{min} value is obtained at Ag layer thicknesses ranging from 45 to 48 nm, as depicted in Fig. 3(b), and for the SM of RI 1.41, the R_{min} value is observed at Ag layer thicknesses ranging from 35 to 48 nm, as shown in Fig. 3(b). Fig. 3(d) shows the reflectance curve, considering R_{min} value at 1, 3, 5, and 7 nm of Ni thicknesses. Maintaining the same thickness, the changes in resonance angle are 10.49°, 11.85°, 13.82°, and 15.85° with 47, 47,47, and 40 nm of Ag thicknesses. Notably, the change in resonance angle is observed to increase with an increase in Ni thickness. Additionally, after increasing the Ni thickness layer, the reflectance curve widens, as shown in Fig. 3(d).

TABLE II
MEASURED PERFORMANCE PARAMETERS FOR DIFFERENT AG AND NI THICKNESS AT R_{min} WITH CONVENTIONAL SENSOR

Ag Thick. (nm)	Ni Thick. (nm)	S (°/RIU)	R_{min} (a.u.) at RI of SM		FWHM (°)	DA (/°)	FoM (/RIU)	LoD (RIU)
			1.33	1.41				
47	1	131.21	2.3×10^{-3}	1.3×10^{-5}	1.91	0.523	68.62	7.6×10^{-6}
47	3	148.21	3.8×10^{-4}	6.8×10^{-5}	2.07	0.483	71.58	6.7×10^{-6}
47	5	172.75	1.6×10^{-4}	4.7×10^{-2}	2.22	0.45	77.73	5.7×10^{-6}
40	7	198.15	6.6×10^{-2}	1.6×10^{-2}	3.05	0.327	64.79	5.0×10^{-6}

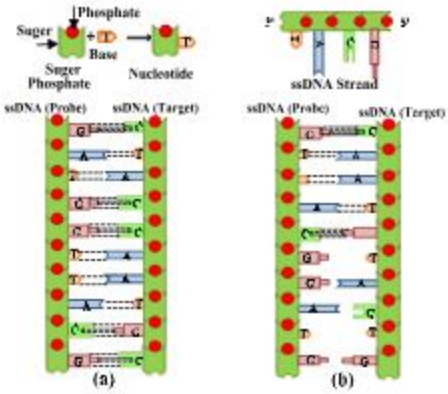

Fig. 4. DNA hybridization events are as follows. (a) Complementary (C) DNA hybridization between pDNA and CT-DNA. (b) Mismatch DNA hybridization between each nucleotide, which is composed of sugar-phosphate and base (adenine, thymine, guanine, and cytosine).

C. DNA Hybridization Detection Analysis Approach

Two polynucleotide strands in DNA are joined to one another by hydrogen bonds, which result from the structure of the double strand helix. Adenine, thymine, cytosine, and guanine are the four distinct repeating nucleotides that make up this molecule. Each nucleotides base in the DNA strand is cross-connected to the base of the nucleotide in the second strand, creating the ladder structure. Adenine can bond exclusively thymine, cytosine can only pair with guanine, and vice versa [43].

These combinations of nucleotide bases form hydrogen bonds that bind DNA strands together. DNA with two single strands will hybridize if their bases are complementary to one another. The detection approach and mathematical equation is given in [1], [34], and [37]. Fig. 4 illustrates the hybridization processes of complementary and mismatched DNA. The probe single strands of DNA (ssDNA) are immobilized on the antimonene surface of the sensor to facilitate DNA hybridization. The complementary target DNA, or CT-DNA, is present in a separate solution and flows over the sensor surface.

P-ssDNA hybridizes with homologous CT-ssDNA, while nonhomologous ssDNA does not bind to either one [36]. Complementary DNA hybridization is the process of attaching two ssDNA that are complementary to one another, creating double stranded DNA (dsDNA). First, we examined the SPR curves characteristic as a bare sensor or without the addition of DNA molecules. The SPR angle shift and R_{min} are necessary for the nucleotide bonding that occurs during dsDNA hybridization resulting from a shift in the RI of varying CT-DNA concentrations.

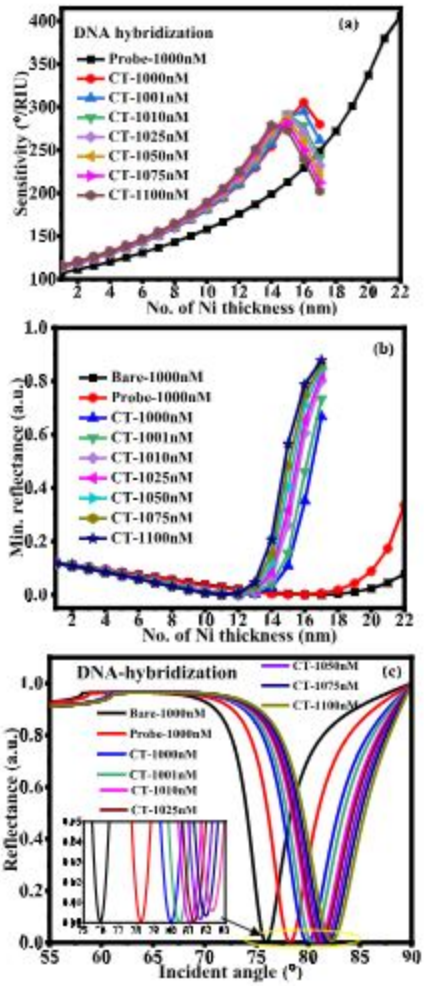

Fig. 5. Sensitivity and R_{min} versus optimized Ni thickness [structure: BAK1 prism-Ag (40 nm)–WS_2 (0.80 nm)–Ni (±nm)–BP (0.53 nm)–SM]. (a) Sensitivity at DNA hybridization concentration. (b) R_{min} at DNA hybridization concentration. (c) Reflectance curve at various concentration of DNA hybridization.

In the detection of DNA hybridization, we have analyzed the variation in thickness of Ni layer of the proposed structure [BAK1/Ag(40 nm)/WS_2/Ni/BP/DNA hybridization]. The reference bare DNA hybridization is considered when computing all the simulation results. The effect of the optimized Ni layer thickness on the sensor's performance parameters, including sensitivity and R_{min} value, is evaluated and shown in Fig. 5(a) and (b). The maximum sensitivity, reaching 379.69°/RIU and 383.01°/RIU, is obtained for p-DNA and mismatch DNA hybridization. Fig. 5(c) shows the reflectance curve for all DNA hybridization on the BP surface. There

TABLE III

MEASURED PERFORMANCE PARAMETERS AT R_{min} WITH DNA-HYBRIDIZATION CONCENTRATION [STRUCTURE: BAK1 PRISM-AG (40 NM)–WS_2(0.8 NM)–NI (*NM)–BP (0.53 NM)–SM]

DNA-Hybridization with concentration and RI values	Ni-Thick (nm)	S (°/RIU)	R_{min} (a.u.)	FWHM (°)	DA (/°)	FoM (/RIU)	LoD (RIU)
Bare-1000nM (RI-1.334)	16	Ref.	6.3×10^{-4}	4.29	0.233	Ref.	Ref.
Probe-1000nM (RI-1.344)	16	229.41	4.4×10^{-4}	4.81	0.207	47.48	4.35×10^{-8}
Mismatch-1000nM (RI-1.3446)	16	230	6.2×10^{-4}	4.85	0.206	47.51	4.49×10^{-8}
CT-1000nM (RI-1.3683)	12	210.14	3×10^{-4}	5.36	0.186	39.08	1.63×10^{-7}
CT-1001nM (RI-1.37)	12	211.08	1.5×10^{-3}	5.49	0.182	38.41	1.71×10^{-7}
CT-1010nM (RI-1.372)	12	215.35	3.3×10^{-4}	5.65	0.176	37.9	1.76×10^{-7}
CT-1025nM (RI-1.3728)	12	217.19	7.9×10^{-4}	5.7	0.175	38	1.78×10^{-7}
CT-1050nM (RI-1.3739)	12	219.82	1.8×10^{-3}	5.79	0.172	37.8	1.81×10^{-7}
CT-1075nM (RI-1.3749)	12	222.34	3.3×10^{-3}	5.88	0.17	37.79	1.83×10^{-7}
CT-1100nM (RI-1.376)	12	225.28	5.8×10^{-3}	5.97	0.167	37.62	1.86×10^{-7}

TABLE IV

MEASURED PERFORMANCE PARAMETERS BELOW AT 0.3 (A.U.) R_{min} WITH DNA-HYBRIDIZATION CONCENTRATION [STRUCTURE: BAK1 PRISM-AG (40 NM)–WS_2(0.8 NM)–NI (7 NM)–BP (0.53 NM)–SM]

DNA-Hybridization with concentration and RI values	Ni-Thick (nm)	S (°/RIU)	Rmin (a.u.)	FWHM (°)	DA (/°)	FoM (/RIU)	LoD (RIU)
Bare-1000nM (RI-1.334)	21	Ref.	0.044	5.07	0.197	Ref.	Ref.
Probe-1000nM (RI-1.344)	21	379.69	0.172	5.45	0.183	69.48	2.63×10^{-6}
Mismatch-1000nM (RI-1.3446)	21	383.01	0.191	5.39	0.185	70.85	2.61×10^{-6}
CT-1000nM (RI-1.3683)	15	285.10	0.108	6.04	0.165	47.04	3.51×10^{-6}
CT-1001nM (RI-1.37)	15	288.08	0.155	5.79	0.172	49.54	3.47×10^{-6}
CT-1010nM (RI-1.372)	15	291.78	0.260	5.01	0.199	58.06	3.43×10^{-6}
CT-1025nM (RI-1.3728)	14	268.67	0.085	6.13	0.163	43.79	3.72×10^{-6}
CT-1050nM (RI-1.3739)	14	273.03	0.115	6.01	0.166	45.32	3.66×10^{-6}
CT-1075nM (RI-1.3749)	14	276.49	0.152	5.81	0.172	47.55	3.62×10^{-6}
CT-1100nM (RI-1.376)	14	279.01	0.206	5.44	0.183	51.05	3.58×10^{-6}

is no vast change in the resonance angle on the addition of noncomplementary target DNA to immobilized pDNA on the BP surface of the biosensor.

The resonance curve is plotted as corresponding Table III. It is observed that as the DNA concentration increases, the FoM decreases. As depicted in Table III, the acquired data highlight the significance of R_{min}, sensitivity, and resonance angle as important factors in the detection of DNA-DNA hybridization. The hybridization of CT-DNAs with P-DNAs modifies these parameters, and the resultant change in resonance angle and R_{min} determines the outcome. Table IV displays the sensitivity and other performance parameter values for the different concentrated CT-DNAs. An increased concentration strongly depends on the resonance angle, according to the numerical data. When the CT-DNA molecules react with the BP surfaces, they create an n-doping effect, which causes the resonance angle shift. The sensitivity to the target DNA molecules hybridization is evident in the data in Table IV, illustrating how sensitivity and R_{min} vary in response to different concentrated CT-DNA additions.

D. Electric Field Intensity and SPPs Mode Analysis Approach

Additionally, the field normalize at various layer interfaces of the proposed biosensor is examined utilizing the COMSOL Multiphysics simulation software. Initially, the transverse component of the normalized electric field is displayed along the distance from the BAK1 prism to the SM, as depicted in Fig. 6(a). The penetration depth (PD) is assessed that can be determined as the distance from the peak value to 37% of field intensity. At the BP–SM interface, the normalized electric field amplitude reaches its maximum and then exponentially decreases into the SM. Consequently, the proposed biosensor's

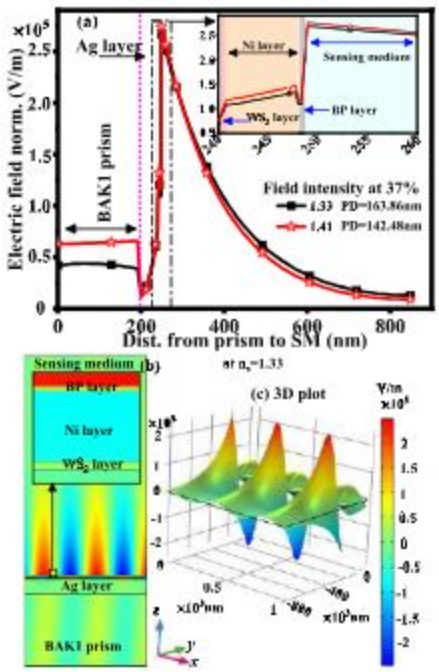

Fig. 6. (a) Electric field normalized at n_s = 1.33 and 1.41, (b) 2-D, and (c) 3-D plot of SPP mode.

TABLE V
MEASURED PERFORMANCE PARAMETERS AT R_{min} WITH DNA-HYBRIDIZATION CONCENTRATION [STRUCTURE: BAK1 PRISM-A G (40 NM)–WS_2(0.8 NM)–NI (NM)–BP(0.53 NM)–SM]

DNA-Hybridization with concentration and RI values	Ni-Thick (nm)	Max. Electric field Intensity (V/m)	PD at 37% field intensity (nm)	PD at 10% field intensity (nm)
1.33	7	268162	163.86	387.42
1.41	7	275489	142.48	346.93
Bare-1000nM (RI-1.334)	16	293745	136.16	316.68
Probe-1000nM (RI-1.344)	16	293634	134.14	311.92
CT-1000nM (RI-1.3683)	12	285482	139.22	323.05
CT-1001nM (RI-1.37)	12	286225	138.89	322.77
CT-1010nM (RI-1.372)	12	286254	138.53	321.98
CT-1025nM (RI-1.3728)	12	286274	138.53	321.73
CT-1050nM (RI-1.3739)	12	286221	138.24	321.3
CT-1075nM (RI-1.3749)	12	286060	137.03	320.91
CT-1100nM (RI-1.376)	12	285805	137.87	320.55

TABLE VI
COMPARISON BETWEEN THE PROPOSED SENSOR AND EXISTING SENSORS

Author and ref.	Wavelength	S (°/RIU)	Year
Pal et al.[37]	633	125	2018
Singh et al. [1]	633	202.37	2020
El-assar et al. [35]	633	208	2023
Proposed work	633	379.69 for probe 383.01 for mismatch	2024

sensitivity is determined by the magnitude of the electric field at the BP–SM interface. Enhancing the electric field intensity at this interface is accountable for the increased sensitivity of the proposed biosensor. Moreover, to enhance the electric field, WS_2 and BP layers keep the Ag layer away from oxidation [44]. The maximum electric field intensity of 2.68×10^5 and 2.75×10^5 V/m is achieved for the SM's RIs of 1.33 and 1.41. Furthermore, the PD corresponding to field decay at 10% and 37% field intensity is depicted in Table V. The plots of 1-D, 2-D, and 3-D for the proposed biosensor are displayed in Fig. 6(a)–(c), showing the electric field normalized and variation of the y-component of SPPs along the layer's interface.

The RI shift is the result of the interaction between the SPPs mode and the SM. The SPP mode essentially consists of SPW propagating through the proposed sensor's interface constituent layers. Light interaction with the Ag-WS_2/Ni/BP/SM surface excites the SPP mode, which is distinguished by its resonance angle and field intensity. The SPP mode is highly sensitive to the RI of the BP–SM, and this sensitivity is exploited for DNA-hybridization detection and other applications.

Finally, a comparison has been conducted between the sensitivity of the proposed biosensor and an existing DNA hybridization-based biosensor, as shown in Table VI. The results indicate that the maximum sensitivity is achieved by the proposed biosensor.

IV. CONCLUSION

This article proposes an SPR biosensor, employing Ag/WS_2/Ni/BP layers. The proposed biosensor has been numerically investigated using TMM and Fresnel equation. The remarkable sensitivity and FoM of 198.15°/RIU and 64.79/RIU are archived at R_{min} value with RI of SM 1.33–1.41. The effects of adding Ni layer are examined with a focus on sensitivity, DA, FoM, and LOD. The maximum sensitivities of 379.69°/RIU, 383.01°/RIU, 285.10°/RIU, 288.08°/RIU, 291.78°/RIU, 268.67°/RIU, 273.03°/RIU, 276.49°/RIU, and 279.01°/RIU are obtained with various DNA hybridization concentrations. The corresponding FoM and LOD values are calculated and presented in Tables II and III in the results section. This work explores the effect of increasing Ni thickness on performance parameters, discussing the enhanced biosensor performance. Numerical investigations reveal that the sensitivity for mismatched DNA hybridization is maximum, providing robust detection across various CT-DNA strands.

REFERENCES

[1] M. K. Singh, S. Pal, A. Verma, Y. K. Prajapati, and J. P. Saini, "Highly sensitive antimonene-coated black phosphorous-based surface plasmon-resonance biosensor for DNA hybridization: Design and numerical analysis," *J. Nanophotonics*, vol. 14, no. 4, p. 046015, 2020.

[2] C. Singhal, M. Khanuja, N. Chaudhary, C. S. Pundir, and J. Narang, "Detection of chikungunya virus DNA using two-dimensional MoS_2 nanosheets based disposable biosensor," *Sci. Rep.*, vol. 8, no. 1, pp. 1–11, May 2018, doi: 10.1038/s41598-018-25824-8.

[3] M. S. Rahman, M. R. Hasan, K. A. Rikta, and M. S. Anower, "A novel graphene coated surface plasmon resonance biosensor with tungsten disulfide (WS_2) for sensing DNA hybridization," *Opt. Mater.*, vol. 75, pp. 567–573, Jan. 2018, doi: 10.1016/j.optmat.2017.11.013.

[4] M. B. Hossain et al., "Hybrid structure based high performance SPR sensor: A numerical approach of structure optimization for DNA hybridization," *Opt. Quantum Electron.*, vol. 53, no. 1, pp. 1–19, Jan. 2021, doi: 10.1007/s11082-020-02650-9.

[5] Y. Vasimalla, H. S. Pradhan, and R. J. Pandya, "SPR performance enhancement for DNA hybridization employing black phosphorus, silver, and silicon," *Appl. Opt.*, vol. 59, no. 24, p. 7299, 2020, doi: 10.1364/ao.397452.

[6] Z. S. Tabatabaeian, F. Kazemi, and S. Ebrahimi, "Plasmonic fractal metasurface with Fano response for virus detection in the optical spectrum," *Opt. Mater.*, vol. 150, Apr. 2024, Art. no. 115153, doi: 10.1016/j.optmat.2024.115153.

[7] F. Kazemi, Z. S. Tabatabaeian, and F. B. Zarrabi, "A terahertz metamaterial biosensor based on spoof surface plasmon polaritons transmission line for avian influenza virus detection," *Opt. Laser Technol.*, vol. 174, Jul. 2024, Art. no. 110694, doi: 10.1016/j.optlastec.2024.110694.

[8] B. Liedberg, C. Nylander, and I. Lunström, "Surface plasmon resonance for gas detection and biosensing," *Sens. Actuators*, vol. 4, pp. 299–304, Jan. 1983, doi: 10.1016/0250-6874(83)85036-7.

[9] M. B. Hossain, T. B. A. Akib, L. F. Abdulrazak, and M. M. Rana, "Numerical modeling of graphene-coated fiber optic surface plasmon resonance biosensor for BRCA1 and BRCA2 genetic breast cancer detection," *Opt. Eng.*, vol. 58, no. 3, Mar. 2019, Art. no. 37104.

[10] R. B. M. Schasfoort, *Handbook of Surface Plasmon Resonance*. London, U.K.: Royal Society of Chemistry, 2017.

[11] Y. A. Akimov and W. S. Koh, "Resonant and nonresonant plasmonic nanoparticle enhancement for thin-film silicon solar cells," *Nanotechnology*, vol. 21, no. 23, Jun. 2010, Art. no. 235201, doi: 10.1088/0957-4484/21/23/235201.

[12] E. Kretschmann and H. Raether, "Radiative decay of non radiative surface plasmons excited by light," *Zeitschrift Für Naturforschung A*, vol. 23, no. 12, pp. 2135–2136, Dec. 1968, doi: 10.1515/zna-1968-1247.

[13] S. Singh, A. Upadhyay, B. Chaudhary, K. Sirohi, and S. Kumar, "Enhanced Cu-Ni-TiO_2-BP plasmonic biosensor for highly sensitive biomolecule detection and SARS-CoV-2 diagnosis," *IEEE Sensors J.*, vol. 24, no. 1, pp. 254–261, Jan. 2024.

[14] Z. S. Tabatabaeian, F. Kazemi, and F. B. Zarrabi, "Periodic stub implementation with plasmonic waveguide as a slow-wave coupled cavity for optical refractive index sensing," *Sci. Rep.*, vol. 14, no. 1, p. 5175, Mar. 2024, doi: 10.1038/s41598-024-55618-0.

[15] M. Sethi et al., "Influence of distinct baffles type turbulence promoter on the thermohydraulic efficiency of solar air heater: A comprehensive review," *Mater. Today, Proc.*, vol. 72, pp. 1275–1283, Jan. 2023, doi: 10.1016/j.matpr.2022.09.299.

[16] R. Zakaria, M. Mahbub, and C. S. Lim, "Studies of surface plasmon resonance effect on different metallic layers of silver (Ag) and copper (Cu) with molybdenum trioxide (MoO_3) for formaldehyde sensor," *Results Opt.*, vol. 11, May 2023, Art. no. 100374, doi: 10.1016/j.rio.2023.100374.

[17] R. Karlsson, "SPR for molecular interaction analysis: A review of emerging application areas," *J. Mol. Recognit.*, vol. 17, no. 3, pp. 151–161, May 2004, doi: 10.1002/jmr.660.

[18] A. K. Sharma and B. D. Gupta, "On the performance of different bimetallic combinations in surface plasmon resonance based fiber optic sensors," *J. Appl. Phys.*, vol. 101, no. 9, May 2007, Art. no. 093111, doi: 10.1063/1.2721779.

[19] P. Kumar, R. Kumar, M. K. Singh, and B. Ahmed, "Detection of plasma, platelets, hemoglobin in blood sample of dengue malaria based on surface plasmon resonance biosensor using black phosphorus: A numerical analysis," *Plasmonics*, pp. 1–12, 2023.

[20] A. Pal et al., "Detecting binary mixtures of sulfolane with ethylene glycol, diethylene glycol, and polyethylene glycol in water using surface plasmon resonance sensor: A numerical investigation," *Plasmonics*, vol. 19, no. 2, pp. 1019–1029, Apr. 2024, doi: 10.1007/s11468-023-02054-x.

[21] J. B. Khurgin and A. Boltasseva, "Reflecting upon the losses in plasmonics and metamaterials," *MRS Bull.*, vol. 37, no. 8, pp. 768–779, Aug. 2012.

[22] I. Pockrand, J. D. Swalen, J. G. Gordon, and M. R. Philpott, "Surface plasmon spectroscopy of organic monolayer assemblies," *Surf. Sci.*, vol. 74, no. 1, pp. 237–244, May 1978.

[23] I. Pockrand, "Surface plasma oscillations at silver surfaces with thin transparent and absorbing coatings," *Surf. Sci.*, vol. 72, no. 3, pp. 577–588, Apr. 1978.

[24] M. I. A. Isti et al., "Asymmetrical D-channel photonic crystal fiber-based plasmonic sensor using the wavelength interrogation and lower birefringence peak method," *Results Phys.*, vol. 19, Dec. 2020, Art. no. 103372.

[25] H. Fu, S. Zhang, H. Chen, and J. Weng, "Graphene enhances the sensitivity of fiber-optic surface plasmon resonance biosensor," *IEEE Sensors J.*, vol. 15, no. 10, pp. 5478–5482, Oct. 2015, doi: 10.1109/JSEN.2015.2442276.

[26] K. Kato et al., "Surface plasmon resonance properties and gas response in porphyrin Langmuir–Blodgett films," *Colloids Surf. A, Physicochemical Eng. Aspects*, vols. 198–200, pp. 811–816, Feb. 2002, doi: 10.1016/s0927-7757(01)01006-8.

[27] M. Pumera, "Graphene in biosensing," *Mater. Today*, vol. 14, nos. 7–8, pp. 308–315, Jul./Aug. 2011.

[28] J. Homola, "Present and future of surface plasmon resonance biosensors," *Anal. Bioanal. Chem.*, vol. 377, no. 3, pp. 528–539, Oct. 2003, doi: 10.1007/s00216-003-2101-0.

[29] Z. S. Tabatabaeian and F. B. Zarrabi, "Self-similar ring element array develop for Fano response as mid-infrared: Liver cancer study," *Opt. Commun.*, vol. 555, Mar. 2024, Art. no. 130263, doi: 10.1016/j.optcom.2023.130263.

[30] A. Nazary, S. Ebrahimi, and A. S. Arezoomand, "Design nano cluster high Q-factor perfect plasmonic absorber for bacteria detection in the optical range," *Optik*, vol. 300, Apr. 2024, Art. no. 171652, doi: 10.1016/j.ijleo.2024.171652.

[31] R. Kumar, S. Pal, Y. K. Prajapati, S. Kumar, and J. P. Saini, "Sensitivity improvement of a MXene- immobilized SPR sensor with Ga-doped-ZnO for biomolecules detection," *IEEE Sensors J.*, vol. 22, no. 7, pp. 6536–6543, Apr. 2022, doi: 10.1109/JSEN.2022.3154099.

[32] L. Han, Z. Chen, T. Huang, H. Ding, and C. Wu, "Sensitivity enhancement of Ag-ITO-TMDCs-graphene nanostructure based on surface plasmon resonance biosensors," *Plasmonics*, vol. 15, no. 3, pp. 693–701, Jun. 2020, doi: 10.1007/s11468-019-01079-5.

[33] P. Kumar, R. Kumar, M. K. Singh, and B. Ahmed, "A highly sensitive surface plasmon resonance sensor based on black phosphorus in the visible regime," *Opt. Quantum Electron.*, vol. 55, no. 12, p. 1101, Nov. 2023, doi: 10.1007/s11082-023-05419-y.

[34] M. B. Hossain, "Numerical modeling of MoS_2-graphene bilayer-based high-performance surface plasmon resonance sensor: Structure optimization for DNA hybridization," *Opt. Eng.*, vol. 59, no. 10, Oct. 2020, Art. no. 105105, doi: 10.1117/1.oe.59.10.105105.

[35] M. El-assar, T. E. Taha, F. E. A. El-Samie, H. A. Fayed, and M. H. Aly, "Zinc selenide based dual-channel SPR optical biosensor for HIV genome DNA hybridization detection," *Opt. Quantum Electron.*, vol. 55, no. 13, p. 1143, Dec. 2023, doi: 10.1007/s11082-023-05296-5.

[36] M. F. O. Hameed, A. S. Saadeldin, E. M. A. Elkaramany, and S. S. A. Obayya, "Label-free highly sensitive hybrid plasmonic biosensor for the detection of DNA hybridization," *J. Lightw. Technol.*, vol. 35, no. 22, pp. 4851–4858, Nov. 1, 2017.

[37] S. Pal, A. Verma, S. Raikwar, Y. K. Prajapati, and J. P. Saini, "Detection of DNA hybridization using graphene-coated black phosphorus surface plasmon resonance sensor," *Appl. Phys. A, Solids Surf.*, vol. 124, pp. 1–11, 2018.

[38] R. Tabassum and B. D. Gupta, "Performance analysis of bimetallic layer with zinc oxide for SPR-based fiber optic sensor," *J. Lightw. Technol.*, vol. 33, no. 22, pp. 4565–4571, Nov. 15, 2015.

[39] A. Yadav, A. Kumar, P. Sharan, and M. Mishra, "Highly sensitive bimetallic-metal nitride SPR biosensor for urine glucose detection," *IEEE Trans. Nanobiosci.*, vol. 22, no. 4, pp. 897–903, Oct. 2023, doi: 10.1109/TNB.2023.3246535.

[40] A. H. M. Almawgani et al., "Magnesium oxide and silicon-assisted surface plasmon resonance sensor for gas detection: A performance analysis," *Plasmonics*, pp. 1–13, Jan. 2024.

[41] B. Karki, A. Pal, P. Sarkar, A. Uniyal, and R. B. Yadav, "Gold, MXene, and graphene nanofilm-based surface plasmon resonance sensor for malaria detection," *J. Opt.*, Feb. 2024, doi: 10.1007/s12596-024-01661-z.

[42] B. Karki, A. Uniyal, A. Pal, and V. Srivastava, "Advances in surface plasmon resonance-based biosensor technologies for cancer cell detection," *Int. J. Opt.*, vol. 2022, Sep. 2022, Art. no. 1476254, doi: 10.1155/2022/1476254.

[43] E. Paleček, "Electroactivity of proteins: Possibilities in biomedicine and proteomics," in *Perspectives in Bioanalysis*. Elsevier, 2005, pp. 689–750, doi: 10.1016/S1871-0069(05)01019-0.

[44] A. Panda, P. D. Pukhrambam, and G. Keiser, "Performance analysis of graphene-based surface plasmon resonance biosensor for blood glucose and gas detection," *Appl. Phys. A, Solids Surf.*, vol. 126, no. 3, p. 153, Mar. 2020.